Finite Element Model for Wave Propagation Near Shore Based on Extended Boussinesq Equations.

L. PINHEIRO, C.J. FORTES
Hydraulics and Environment Department, Ports Division
National Laboratory for Civil Engineering
Av. do Brasil 101, 1700-066 Lisboa
PORTUGAL
lpinheiro@lnec.pt, jfortes@lnec.pt http://www.lnec.pt
J.A. SANTOS
Civil Engineering Department
Instituto Superior de Engenharia de Lisboa
Rua Conselheiro Emídio Navarro 1, 1959-007 Lisboa
PORTUGAL
jasantos@dec.isel.pt http://www.isel.pt
L. FERNANDES
Mechanical Engineering Department
Instituto Superior Técnico
Av. Rovisco Pais, 1 1049-001 Lisboa
PORTUGAL
leonel@dem.ist.utl.pt http://www.ist.utl.pt
M. WALKLEY
School of computing
Leeds University
Leeds
UK
m.a.walkley@leeds.ac.uk http://www.comp.leeds.ac.uk

Abstract: - This paper describes the numerical model BOUSS-WMH (BOUSSinesq Wave Model for Harbours), a finite element model for nonlinear wave propagation near shore and into harbors. It is based upon an extended version of the Boussinesq equations to which terms were added to generate regular or irregular waves inside the numerical domain, absorb outgoing waves, partially reflect waves at physical boundaries, control numerical instabilities and reproduce energy dissipation due to bottom friction and wave breaking. The paper focuses on the implementation of partial reflection, bottom friction and wave breaking as well as on the model applications to experimental test cases. Results are compared with physical model tests and another numerical model.

Key-Words: Wave Propagation, Boussinesq Equations, Harbours, Finite Elements

1. Introduction

The most important physical effects associated with the nonlinear wave transformation of sea waves in nearshore regions can be described by Boussinesq-type equations [19]. One example of this class of equations was introduced by Nwogu [30]. Such equations describe the nonlinear evolution of sea waves over a sloping impermeable bottom without considering wave breaking. Their validity range extends from shallow up to intermediate water depths where the nonlinear and dispersive effects are mild. Therefore, they seem adequate to describe the wave field outside and inside ports, harbours and sheltered zones. In the last few decades several authors have been working to extend the applicability domain of these equations to deep as well as to very shallow waters and also to include other physical phenomena such as currents, wave breaking, bottom friction etc… Nowadays there is a large number of extended Boussinesq equations [26][29][25][5][30][42][13][27][28][1][46][18].

The numerical resolution of Boussinesq-type equations has mostly used finite difference methods [32][26][29][4][43][20][23]. Although computationally more complex, the finite element method deals directly with unstructured grids that correctly represent the physical boundaries of the domain, including the coastline, islands and other obstacles. Moreover the finite element method allows minimizing the number of points in the grid using local refinement techniques. Several authors have used this method with success [15][2][14][3][22][39][40]. These models use different time integration schemes and either triangular or rectangular linear elements. Recent advances in computational resources allow for inclusion of higher levels of non-linear and frequency dispersion terms as well as more complex interpolation functions [45][12].

Developments on Walkey's model [40] led to the BOUSS-WMH model whose first version was presented in Pinheiro *et al.* [33]. The model now includes internal wave generation (using the source function method with which regular and irregular waves can be generated), artificial numerical viscosity (to control numerical instabilities), numerical sponge layers (placed on radiation boundaries to absorb outgoing waves), numerical porosity layers (placed either on physical boundaries or inside the domain to simulate the reflection, transmission and energy dissipation effects of porous structures on the waves) and energy dissipation due to bottom friction and wave breaking.

This paper is organized as follows: in section 2, the governing equations are summarized, the extensions to the original equations are presented and the numerical scheme is briefly discussed. Three different applications of the model are given in Section 3. The simulation of wave propagation over: a spherical shoal to evaluate nonlinear behaviour of the model and test the model's sensitivity to different meshes; a constant slope beach profile and a bared beach profile to evaluate the wave breaking simulation. In the above test cases, the numerical results are compared with results from physical model measurements. The concluding remarks are drawn in the last section.

2. BOUSS-WMH Numerical Model

2.1 Generic model description

The extended Boussinesq equations derived by Nwogu [30] are given by the following equations, at depth $Z_\alpha=\theta h$.

$$\frac{\partial \eta}{\partial t}+\nabla((h+\eta)\mathbf{u})+ +\nabla\cdot\left(\left(\frac{Z_\alpha{}^2}{2}-\frac{h^2}{6}\right)h\nabla(\nabla\cdot\mathbf{u})+\left(Z_\alpha+\frac{h}{2}\right)h\nabla(\nabla\cdot(h\mathbf{u}))\right)=0 \tag{1}$$

$$\frac{\partial \mathbf{u}}{\partial t}+(\mathbf{u}\cdot\nabla)\mathbf{u}+g\nabla\eta+\frac{Z_\alpha{}^2}{2}\nabla\left(\nabla\cdot\frac{\partial \mathbf{u}}{\partial t}\right)+ +Z_\alpha\nabla\left(\nabla\cdot\left(h\frac{\partial \mathbf{u}}{\partial t}\right)\right)=0 \tag{2}$$

where η is the free surface elevation, $\mathbf{u}=\mathbf{u}(x,y,t)=(\mathrm{u},\mathrm{v})$ is the horizontal velocity vector, h the water depth.

The original Nwogu's equations were further extended to take into account some important physical processes (wave transmission through porous structures, bottom friction and wave breaking) as well as other source/damping terms for numerical reasons. The BOUSS-WMH model equations result as follows:

$$\frac{\partial \eta}{\partial t}+\nabla((h+\eta)\mathbf{u})+ +\nabla\cdot\left(\left(\frac{Z_\alpha{}^2}{2}-\frac{h^2}{6}\right)h\nabla(\nabla\cdot\mathbf{u})+\left(Z_\alpha+\frac{h}{2}\right)h\nabla(\nabla\cdot(h\mathbf{u}))\right)= =S_f+(\upsilon_t+\upsilon_s)\nabla^2\eta \tag{3}$$

$$\frac{\partial \mathbf{u}}{\partial t}+(\mathbf{u}\cdot\nabla)\mathbf{u}+g\nabla\eta+\frac{Z_\alpha{}^2}{2}\nabla\left(\nabla\cdot\frac{\partial \mathbf{u}}{\partial t}\right)+ +Z_\alpha\nabla\left(\nabla\cdot\left(h\frac{\partial \mathbf{u}}{\partial t}\right)\right)= =n\mathbf{u}\left(f_l+nf_t|\mathbf{u}|\right)+\frac{1}{h+\eta}\left(f_w\mathbf{u}|\mathbf{u}|+\nabla\upsilon_e\nabla(h+\eta)\mathbf{u}\right) \tag{4}$$

where the added terms stand for:

- S_f - source function for wave generation;
- $(\upsilon_t+\upsilon_s)\nabla^2\eta$ - viscous damping (distribution in time and in space);
- $nf_l\,\mathbf{u}+nf_t\,\mathbf{u}|\mathbf{u}|$ - laminar and turbulent friction (porous structures);
- $\frac{1}{h+\eta}f_w\,\mathbf{u}|\mathbf{u}|$ - wave induced bottom friction;
- $\frac{1}{h+\eta}\nabla\upsilon_e\nabla(h+\eta)\mathbf{u}$ - wave breaking.

These additional terms are detailed in the following sections.

2.2 Wave generation

The wave generation is made by an internal generation condition, which is added to the model, using a source function following the procedure described by Wei *et al.* [41]. In this method, the source function is derived by a linearized form of the Boussinesq equations and by using Green's theorem, an explicit relation between the desired surface wave amplitude and the source function amplitude is obtained. A Gaussian function is used to distribute the generated wave over several mesh points.

$$s_f(x,t) = D \cdot e^{\left(-\sigma \cdot (x_s - x)^2\right)} \cdot \sin(-\omega \cdot t) \tag{5}$$

where D is the amplitude of the source function, σ is a parameter corresponding to the width of the source region and $(x_s–x)^2$ is the square of the distance to the centre of the source region.

$$D = 2 \cdot \eta_0 \cdot \frac{\left(\omega^2 - \alpha_1 \cdot g \cdot k^4 \cdot h^3\right)}{\omega \cdot I_1 \cdot k \cdot \left(1 - \alpha (kh)^2\right)} \tag{6}$$

where $\alpha_1 = \alpha + 1/3$, and I_1 is given by:

$$I_1 = \sqrt{\frac{\pi}{\sigma}} \cdot e^{\left(-\frac{k^2}{4 \cdot \sigma}\right)} \tag{7}$$

2.3 Boundary conditions

The boundary conditions can be of three types: full absorption, full reflection or partial reflection.

Full reflection represents a solid impermeable vertical wall. Non permeability and mass conservation conditions lead to the following boundary conditions:

$$\mathbf{u} \cdot \mathbf{n} = 0 \text{ and } \mathbf{w} \cdot \mathbf{n} = 0 \tag{8}$$

where n is perpendicular to the boundary.

Full absorption is obtained with use of viscous damping layers (sponge layers) This viscous term has quadratic growth in the part of the domain corresponding to the sponge layer absorbing all frequencies of waves, see section *2.4.1.3* for more details.

To partially absorb wave energy at a given boundary the method presented by Nwogu & Dermirbilek [31] is used. It simulates partial wave reflection and also transmission through porous structures such as breakwaters. The modified equations for the porous region are obtained by replacing **u** with **u**/n, where n is the porosity, and including a term to account for energy dissipation inside the structure.

Laminar and turbulent friction factors are obtained using the empirical relationships recommended by Engelund [11]:

$$f_l = \alpha_0 \frac{(1-n)^3}{n^2} \frac{\upsilon}{d^2} \quad \text{and} \quad f_t = \beta_0 \frac{(1-n)}{n^3} \frac{1}{d^2} \tag{9}$$

where υ is the kinematic viscosity of water, d is the characteristic stone size, and α_0 and β_0 are empirical constants that range from 780 to 1500, and 1.8 to 3.6 respectively. The characteristic stone size is given by:

$$d = \left(\frac{W_s}{g \cdot \rho_s}\right)^{1/3} \tag{10}$$

where W_s is the stone weight in kN and ρ_s is the mass density of armor material (2650 kg/m3.for quarry stone and 2300 kg/m3 for concrete blocks).

The region where the partial reflection condition is enforced is a porosity layer and it must be introduced gradually to avoid large discontinuities which lead to instability. So, a Gaussian function is used to distribute growing porosity in half a wavelength width. Fig. 1 shows an example of varying viscosity and porosity.

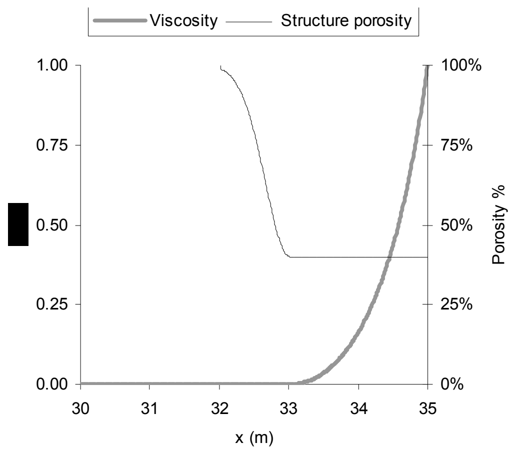

Fig. 1: Viscosity (quadratic growth in sponge layer) and Porosity (Gaussian growth in porous layer).

2.4 Energy dissipation

2.4.1 Viscous damping

The viscous damping term has three components:

$$\nu = \nu_t + \nu_1 + \nu_2 \tag{11}$$

The first component is distributed in time domain. The other two components are distributed in space domain. ν_t and ν_l aim at controlling numerical instabilities while ν_2 aims at absorbing outgoing waves at fully absorptive boundaries.

2.4.1.1. Stability control at initial time steps

Initial conditions for this problem are those for an undisturbed free surface. For this initial condition, as the wave enters the domain, the integration software will identify that as a discontinuity, forcing the use of very small time steps. In order to avoid this, a smoothing function (ν_t) is introduced:

$$\nu_t = m_1 \cdot e^{-m_2 \frac{t}{T}} \tag{12}$$

where T is the wave period and m_1 and m_2 are empiric constants that usually range between 1×10^{-3} and 2×10^{-3} and 0.5 and 2, respectively. This term is added to the free surface equation as a viscous coefficient. In the first time steps this will damp the solution, allowing the use of larger time steps. Due to the exponential decay nature of this damping term, it will not affect the solution obtained after a suitably large time.

2.4.1.2. Stability control in space domain

In order to avoid spurious modes that damp the numerical solution, a small viscosity is introduced equally distributed in space and covering the whole domain. An expression for this viscosity can be given by:

$$\nu_1 = \frac{\gamma \cdot \lambda^4}{(2 \cdot \pi \cdot \Delta x)^3} \tag{13}$$

where λ is the wave length Δx is the average node spacing and γ is an empirical parameter in *m/s* that usually ranges between $2\text{x}10^{-6}$ and 8.5x10-6.

2.4.1.3. Sponge layers

It is important to fully absorb all incident waves at the outgoing boundaries. Due to the dispersive nature of the equations modelled, a simple radiation boundary condition is not completely effective, as the waves in the domain do not have a single phase speed. Therefore, a viscous damping layer, termed sponge layer, is introduced near the outflow boundary in order to absorb incident waves at those boundaries. These sponge layers take the form of a viscous term (ν_2) added the free surface equation as presented in the following equation:

$$\nu_2 = \frac{30}{T} \cdot \frac{e^{\left(\frac{X - X_s}{X_F - X_s}\right)^2} - 1}{e - 1} \tag{14}$$

where, X_S is the starting location of the layer and X_F is its final location. X_F-X_S is the width of the layer. It was found in practice that the width of the sponge layer must be one to two wavelengths, in order to provide sufficient damping, [20].

Viscosity layers must be introduced gradually. So, this viscous term grows quadratically in the part of the domain corresponding to the sponge layer, see Fig. 1.

2.4.2 Bottom friction

The bottom boundary layer of flow associated with the passage of waves is normally restricted to a small region above the sea floor. There is therefore a very small amount of energy dissipation due to bottom friction in typical wave propagation distances of the order of 1km used in Boussinesq-type models. The energy dissipation due to bottom friction however plays an important role in the wave transformations near shore, in very shallow waters.

The effect of energy dissipation due to a turbulent bottom boundary layer is simulated using a term of bottom shear stress, F_b, to the momentum equation, following the procedure adopted by Nwogu & Demirbilek [31].

$$F_b = \frac{1}{h + \eta} f_w U_\alpha |U_\alpha| \tag{15}$$

where f_w is the wave friction factor. This equation is expressed in terms of U_α instead of the bottom velocity in order to minimize the computational effort to determine it.

The wave friction factor estimates the bottom shear stress induced by the passage of the wave. To estimate the wave friction factor the method presented by Le Roux [21] is used. This author proposes a rigorous form of expressing f_w using two variables, the equivalent diameter of the particles, D, and the wave period, T.

$$f_w = \frac{2\beta g \rho_\gamma D}{U_{wcr}^2 \rho} \tag{16}$$

where ρ_γ e ρ are the densities of the submerged particles and of water, respectively. The Shields parameter, β, is given by:

$$\beta = \begin{cases} -0.0717 \log(W_{ds}) + 0.0625 & \Leftarrow W_{ds} < 2.5 \\ 0.0717 \log(W_{ds}) + 0.0272 & \Leftarrow 2.5 < W_{ds} < 11 \\ 0.045 & \Leftarrow W_{ds} > 11 \end{cases} \tag{17}$$

The critical orbital velocity, U_{wcr} is given by:

$$U_{wcr} = -0.002\left(\left(\theta_{wcr} g D \rho_\gamma\right)^2 \frac{T}{\rho\mu}\right) + \\ +1.0702\left(\theta_{wcr} g D \rho_\gamma \left(\frac{T}{\rho\mu}\right)^{0.5}\right) \tag{18}$$

with $\theta_{wcr} = 0.027 W_{ds}^{-0.6757}$, where W_{ds} is the nondimensional sedimentation velocity and can be evaluated according to the empirical formulation of Dietrich [10]:

$$W_{ds} = 0.68 \frac{D^2}{5832} \tag{19}$$

2.4.3 Wave breaking

Wave breaking is a very complex turbulent phenomenon that constitutes an important form of energy dissipation and cannot be neglected in near shore areas.

Several empirical formulations have been adopted by different authors to model wave breaking.

To model the turbulent mixing and dissipation caused by breaking, an "eddy viscosity" approach is used, [18]. It consists in adding an ad-hoc dissipative and momentum conservative term R_b to the momentum equation. This term contains the eddy viscosity, which is defined in agreement with experimental data.

$$R_b = \frac{1}{h+\eta}\frac{\partial}{\partial x}\left(\nu\frac{\partial}{\partial x}\left[(h+\eta)u\right]\right) \tag{20}$$

and ν is the eddy viscosity and $h+\eta$ represents the total water depth. The eddy viscosity is defined as:

$$\nu = B.\delta_b^2.(h+\eta).\left|\frac{\partial\eta}{\partial t}\right| \tag{21}$$

The parameter δ_b is the mixing length coefficient. The purpose of the parameter B is to avoid an impulsive start of the wave breaking and consequently the instability of the solution.

$$B = \begin{cases} 1 & \text{if } \dfrac{\partial\eta}{\partial t} \geq 2.\dfrac{\partial\eta^*}{\partial t} \\ \dfrac{\partial\eta/\partial t}{\partial\eta^*/\partial t} - 1 & \text{if } \dfrac{\partial\eta^*}{\partial t} < \dfrac{\partial\eta}{\partial t} \leq 2.\dfrac{\partial\eta^*}{\partial t} \\ 0 & \text{if } \dfrac{\partial\eta}{\partial t} \leq \dfrac{\partial\eta^*}{\partial t} \end{cases} \tag{22}$$

where $\partial\eta^*/\partial t$ determines the onset and the cessation of wave breaking. The use of $\partial\eta/\partial t$ as an initiation parameter ensures that the dissipation is concentrated in the front face of the wave as in nature.

A breaking event begins when $\partial\eta/\partial t$ exceeds some initial threshold value and it will continue even if $\partial\eta/\partial t$ drops bellow that value. The magnitude of the threshold value will decrease in time from the initial value $\partial\eta^{(I)}/\partial t$ to a final one $\partial\eta^{(F)}/\partial t$. A simple linear relation is used to model the evolution of $\partial\eta^*/\partial t$:

$$\frac{\partial\eta^*}{\partial t} = \begin{cases} \dfrac{\partial\eta^{(I)}}{\partial t} & \text{if } t-t_0 \leq 0 \\ \dfrac{\partial\eta^{(F)}}{\partial t} & \text{if } t-t_0 \geq T^* \\ \dfrac{\partial\eta^{(I)}}{\partial t} + \dfrac{t-t_0}{T^*}\left(\dfrac{\partial\eta^{(F)}}{\partial t} - \dfrac{\partial\eta^{(I)}}{\partial t}\right) & \text{if } 0 \leq t-t_0 < T^* \end{cases} \tag{23}$$

where T^* is the transition time, t_0 is the instant where breaking was initiated and so $t-t_0$ is the age of the wave breaking event. The expressions for $\partial\eta^{(I)}/\partial t$, $\partial\eta^{(F)}/\partial t$ and T^* are:

$$\frac{\partial\eta^{(I)}}{\partial t} = ini * \sqrt{g.H_a} \tag{24}$$

$$\frac{\partial\eta^{(F)}}{\partial t} = fin * \sqrt{g.H_a} \tag{25}$$

$$T^* = tcst * \sqrt{H_a/g} \tag{26}$$

These parameters must be correctly calibrated in order to simulate well the wave breaking.

3. Applications

The model was applied to three different test cases: a) regular waves that propagate over a spherical shoal, b) wave propagation at an experimental beach profile and c) wave propagation over a bared beach.

The numerical simulations were run in a LINUX workstation with a quad-core AMD Opteron™ 265 at 2GHz and 8GB RAM memory.

Comparisons with experimental and numerical results were made using three statistical parameters: the agreement index, AI [44], the quadratic mean error (RMSE) and the absolute mean error (BIAS), each given by equations:

$$AI = 1 - \frac{\sum_{i=1}^{n}\left|y_i - x_i\right|^2}{\sum_{i=1}^{n}\left(\left|y_i - \bar{x}\right| + \left|x_i - \bar{x}\right|\right)^2} \tag{27}$$

$$RMSE = \sqrt{\frac{\sum_{i=1}^{n}\left(y_i - x_i\right)^2}{N}} \tag{28}$$

$$BIAS = \frac{\sum_{i=1}^{n}\left(y_i - x_i\right)}{N} \tag{29}$$

where x_i are the experimental values, y_i are the numerical model values, $\bar{x}$ is the average experimental value and N is the number of points. The agreement index ranges from 0 to 1, being 1 the maximum agreement between experimental and numerical values.

3.1 Spherical shoal

This test case helps to evaluate nonlinear behaviour of the model as well as the model's sensitivity to different mesh sizes.

3.1.1 Numerical conditions

The case of propagation of waves over a spherical shoal was studied experimentally and numerically by Chawla [7]. Chawla performed a number of physical simulations with both regular and irregular waves.

In Fig. 2 the geometry of the shoal and transects, where measurements were made are presented. The wave tank is 20 m long and 18.2 m wide with a maximum and minimum depth of 0.45 m and 0.08 m respectively. The centre of the shoal is located at x=5.0 m and y=8.98 m. The shoal is a portion of a sphere with 9.1 m radius and the circular intersection of the shoal and the bottom is given by:

$$(x-7)^2+(y-8.98)^2=2.57^2 \tag{30}$$

The equation that describes the bathymetry inside this circle is:

$$z=-9.18+\sqrt{8.98^2-(x-7)^2-(y-8.98)^2} \tag{31}$$

where z coordinate has its origin at the still water surface.

Test cases 1, 2 and 3 proposed by Chawla [7] are simulated here. In Table 1 the wave characteristics and kh for the fundamental wave as well as for the 1st and 2nd harmonics are presented. Wave breaking does not occur in any of the three test cases. Kh parameter indicates that Boussinesq type models can represent nonlinear wave interactions although 2nd harmonics have relatively high values, especially for cases 1 and 2.

Test	H(m)	T(s)	L(m)	kh(1)	kh(2)	kh(3)
1	0.019	0.75	0.875	3.21	12.85	51.41
2	0.040	0.75	0.875	3.21	12.85	51.41
3	0.023	1.00	1.490	1.90	7.25	16.63

Table 1: Wave characteristics for the spherical shoal case.

The numerical domain, wave generation line and two sponge layers with increasing viscosity are shown in Fig. 14. The generation zone is located at y = 3 m and is 0.89 m wide. All the boundaries of the domain are fully reflective but two sponge layers were placed at both outgoing boundaries. These sponge layers are 1.78 m wide. The time step was of 0.01 s and the total simulation time was of 40 s.

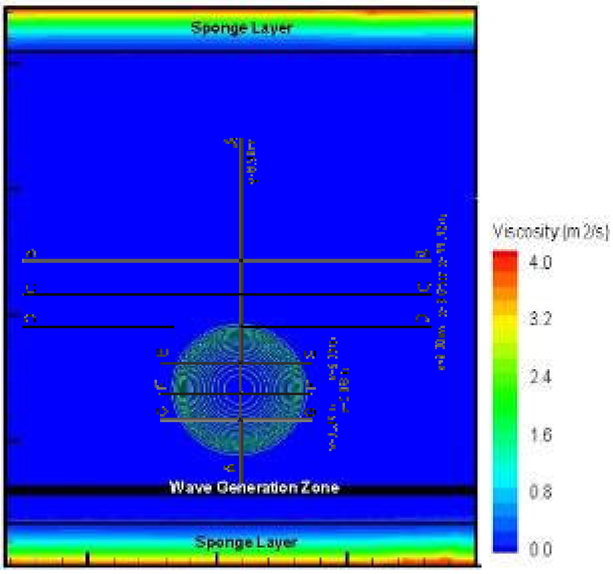

Fig. 2: Geometric configuration of the tank.

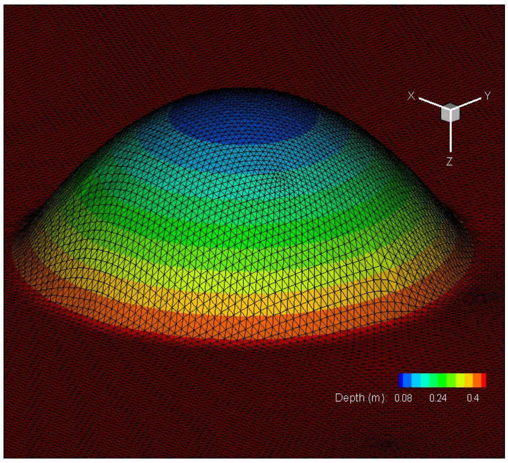

Fig. 3: 3D perspective of the shoal and the mesh.

For the above three incident conditions, the model BOUSS-WMH was applied. The results in terms of significant wave height were compared with experimental results as well as with numerical results from another Boussinesq-type model, COULWAVE, [23], that is more accurate than BOUSS-WMH and uses finite differences.

3.1.2 Sensitivity analysis

To evaluate the influence of the finite element mesh size on the numerical results, five different meshes were generated ranging in number of points from about 18 000 to 300 000 - this corresponds to an average of 5 to 21 points per wavelength (Np/λ), for a wave period of T = 0.75 s. The meshes bandwidths (BW) vary between 187 and 744. In terms of quality, 86% to 99.96% of the elements are considered optimal (i.e. each node is connected to six other nodes and the triangles' internal angles are 60º). In Table 2 the mesh characteristics are presented.

Mesh	Np	Ne	BW	Np/λ		Np_{min}/ λ	
				0.75s	1s	0.75s	1s
A	18169	35840	187	5	11	3	7
B	31204	61910	290	7	16	3	7
C	72140	143286	376	10	24	6	14
D	144207	287388	709	16	37	8	18
E	287614	573242	744	21	48	11	25

Table 2: Finite element meshes characteristics for spherical shoal example.

The values of the significant wave height index (the ratio between significant wave height of a point in the area and height of incident wave) are then calculated at the whole domain but specifically at 60 points distributed along transects A-A to G-G, for comparison with the physical model results.

Fig. 16 shows the significant wave height indexes at transect A-A obtained for all meshes, for tests 2 and

3. Fig. 17 shows a comparison of statistical parameters, *AI*, *RMSE* and *BIAS* which characterize the differences in relation to experimental results, and the processing time (CPU time) obtained by the different meshes.

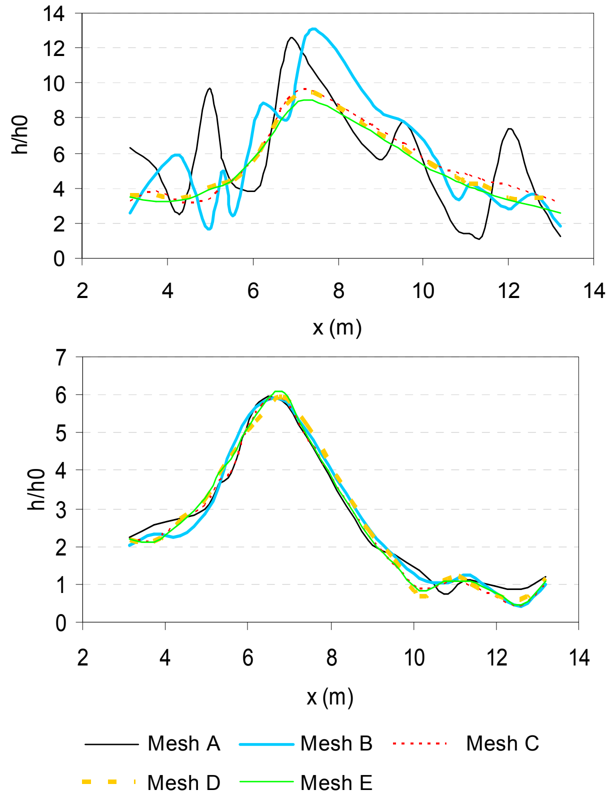

Fig. 4: BOUSS-WMH model. Significant wave height indexes for each grid. Test 2 (above) Test 3(below).

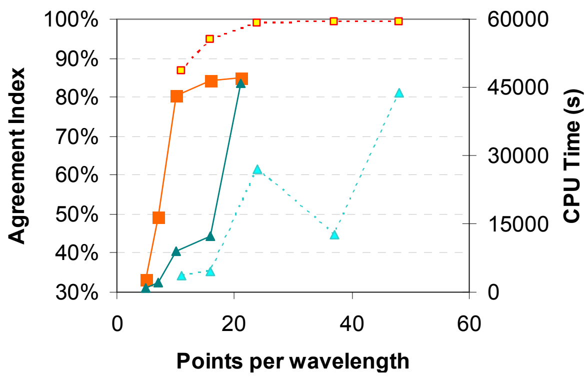

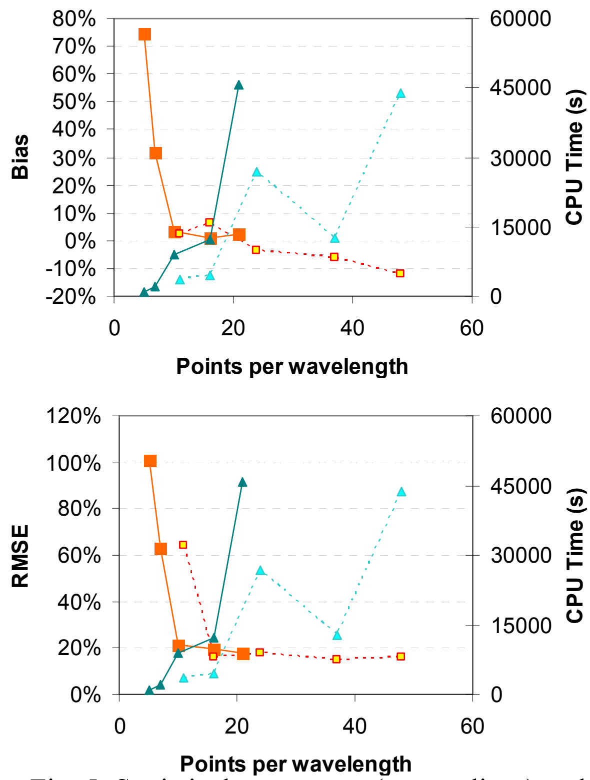

Fig. 5: Statistical parameters (orange lines) and CPU time (blue lines) evolution with the mesh size. (Dashed line - Test 2; solid line - Test 3).

In test 3, it is observed that from grid C to F, the numerical differences in results are minor. In test 2, which is a more demanding test than test 3 (higher non-linearity), only grids D and E have satisfactory results. So, it can be concluded that the model requires a minimum of 6 and an average of 10 points per wavelength to obtain acceptable results. However, only from a minimum of 8 and an average 16 points per wavelength are the results more accurate (Grid D). Taking the smallest processing time required to obtain a reasonable accuracy on results, it appears that the D grid is the best to simulate the other tests.

3.1.3 Results

For the three tests, using mesh D, comparisons of the numerical model results with the experimental data [7] and numerical results from the COULWAVE model [23] are presented.

Statistical parameters (AI, RMSE *and* BIAS) are used to quantify the differences in the significant wave heights for all sections. The energy spectra obtained by numerical models for three gauges located in transect A-A were also calculated.

3.1.3.1. Free surface elevation and wave height indexes

A 3D visualization of the numerical values of the free surface elevation after 5 s, 10 s, 20 and 40 s of simulation for test 2 (T = 0.75 s, H = 0.4 m) is shown, *Fig. 1*. *Fig. 2* and *Fig. 3* presents the views of 2D free surface elevation after 40 s of simulation and a 3D view of the detail located over the shoal. *Fig. 4* shows the contours of the wave height indexes 40 s of simulation, for tests 1, 2 and 3.

Fig. 1 clearly shows the propagation of the waves over time on the spherical shoal. There are changes in the wave (direction, height and shape) due to the effects of bottom induced refraction and wave diffraction around the shoal. Indeed, the wave as it passes over the shoal suffers: a) the shoaling due to decrease in depth, b) refraction due to the orientation of the bathymetry c) diffraction due to the presence of the shoal that is somewhat of an obstacle that the wave must overcome. This leads to an increase in wave height after the shoal, as this is an area where the waves that skirted the shoal will meet (area of energy concentration) as well as reducing the height on each side of the shoal due to the lateral distribution of energy (diffraction). This behavior is also displayed in *Fig. 2* and *Fig. 3*. In the latter figure it is also visible the high non-linearity of the waves, since they have sharp crests and flattened troughs.

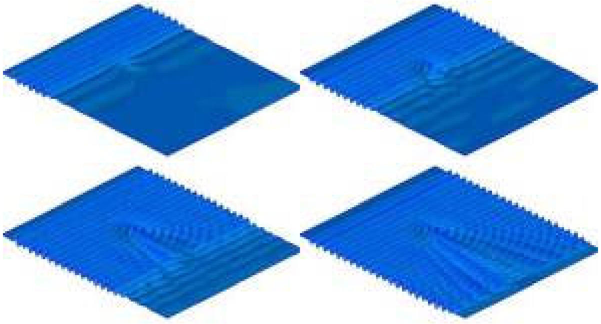

Fig. 1. Free surface elevation after 5 s, 10 s, 20 s e 40 s of simulation (Test 2).

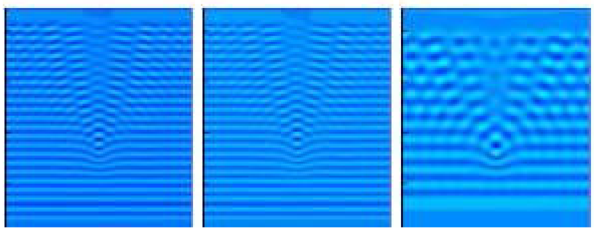

Fig. 2. Free surface elevation after 40 s of simulation. Tests 1, 2 and 3, respectively.

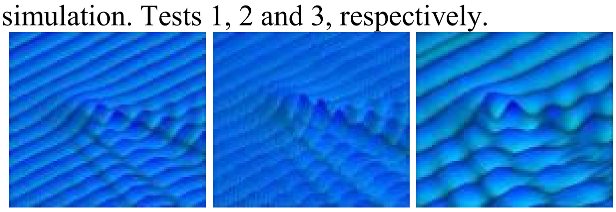

Fig. 3. Free surface elevation detail over the shoal after 40 s of simulation. Tests 1, 2 and 3, respectively.

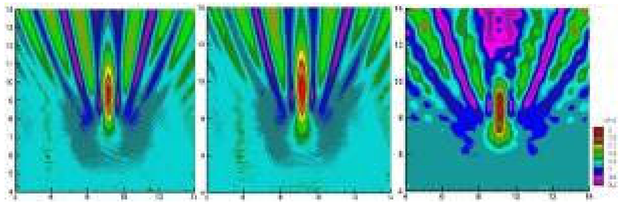

Fig. 4. BOUSS-WMH – Contour plots of wave height indexes. Tests 1, 2 and 3, respectively.

The pattern of wave height indexes is very similar for all three test cases. Before the shoal no significant differences of the i wave height indexes occur, over the shoal there is a progressive increase of these values and they reach a maximum value immediately after the shoal. The extent of this zone of high values varies from test to test. After this zone, there is a decrease of the wave height indexes. On the sides (left and right) of the shoal there is a decrease of wave height indexes.

Comparing the wave height indexes of the tests 1 and 2 whose main difference is the height of the incident wave, it appears that the zone of increased wave height stretches for an area larger for test 2 than test 1. For the third test, this area has an even greater extent, since the period of the incident wave of this case is larger. Thus, the wave feels the presence of the shoal sooner than in the other two cases. It also turns out a better definition of contour lines (less noise) is a consequence of a greater number of points per wavelength of the finite element mesh.

3.1.3.2. Significant wave heights

Fig. 6, Fig. 7 and Fig. 8 show the numerical significant wave heights obtained by the models BOUSS-WMH and COULWAVE and the experimental values in transects A-A, C-C and G-G, for tests 1, 2 and 3. The corresponding statistical parameters are shown in Table 3,Table 4 and Table 5.

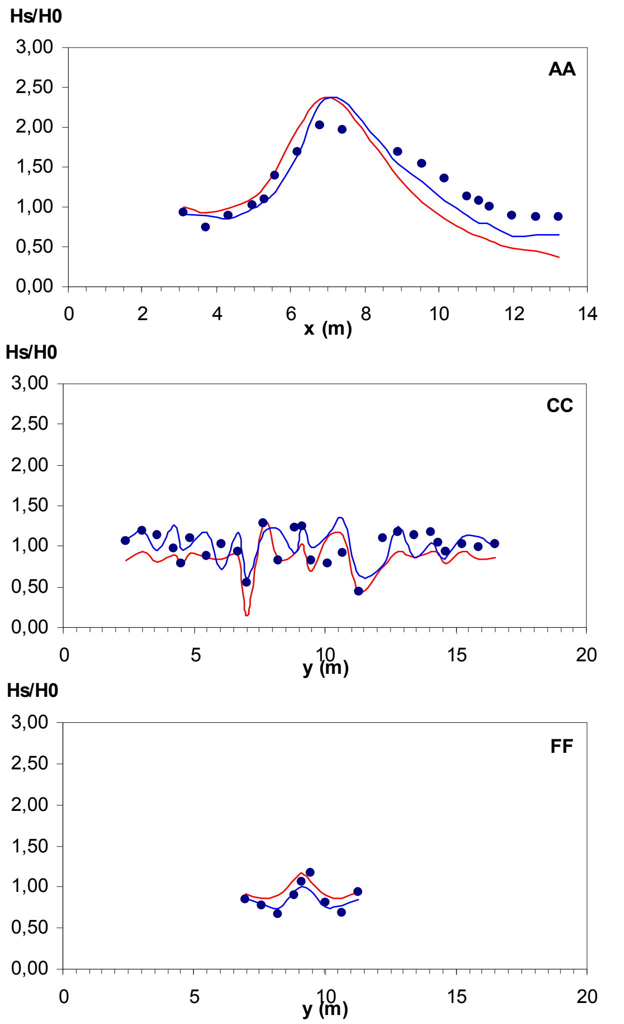

Fig. 6 - Test 1. Transects A-A, C-C and F-F. Wave height indexes. Experimental (black points) and numerical values: BOUSS-WMH (blue), COULWAVE (red).

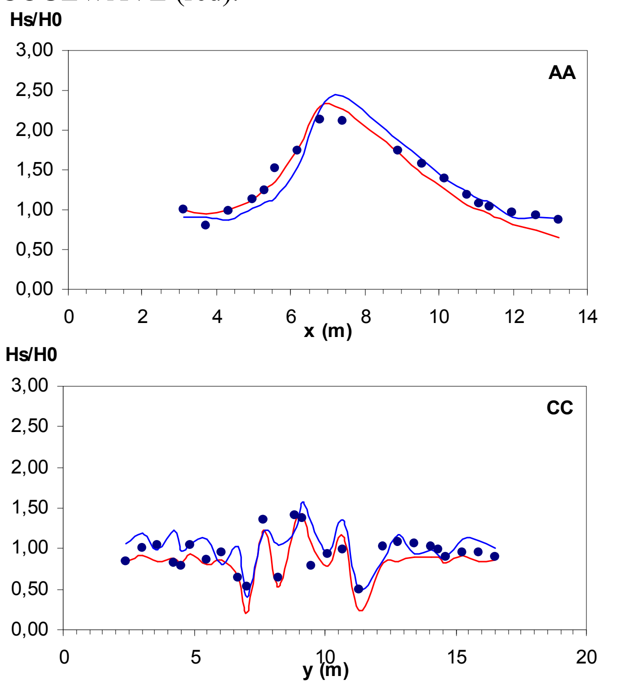

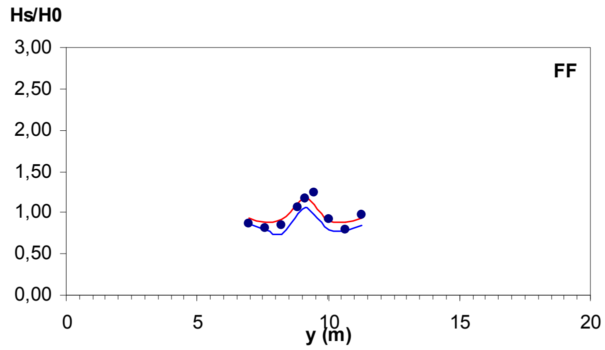

Fig. 7 - Test 2. Transects A-A, C-C and F-F. Wave height indexes. Experimental (black points) and numerical values: BOUSS-WMH (blue), COULWAVE (red).

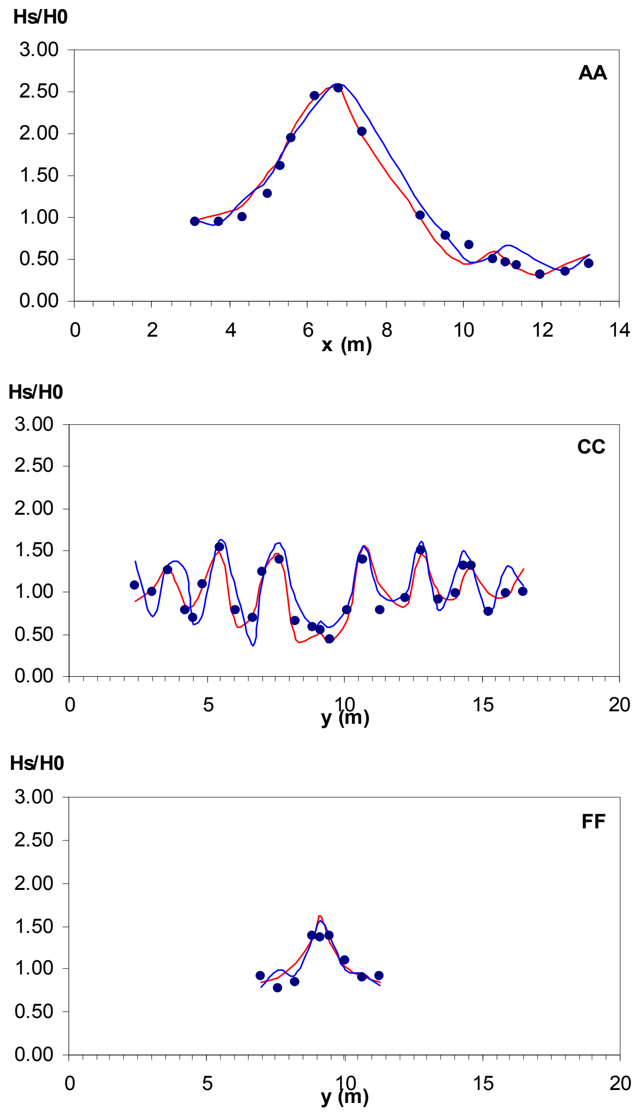

Fig. 8 - Test 3. Transects A-A, C-C and F-F. Wave height indexes. Experimental (black points) and numerical values: BOUSS-WMH (blue), COULWAVE (red).

	BIAS		RMSE		AI	
	CW	BSS	CW	BSS	CW	BSS
AA	-0.111	-0.279	0.571	0.312	0.712	0.867
BB	-0.061	-0.220	0.630	0.536	0.443	0.450
CC	-0.010	-0.134	0.456	0.293	0.387	0.600
DD	-0.055	-0.197	0.479	0.305	0.498	0.806
EE	0.150	-0.263	0.251	0.200	0.870	0.858
FF	0.222	-0.160	0.211	0.132	0.589	0.630
GG	0.063	-0.210	0.079	0.156	0.362	0.406

Table 3: Test 1. Transects A-A to G-G. Statistical parameters.

	BIAS		RMSE		AI	
	CW	BSS	CW	BSS	CW	BSS
AA	-0.649	0.013	0.729	0.186	0.543	0.954
BB	-0.385	0.125	0.661	0.389	0.396	0.620
CC	-0.370	0.128	0.573	0.261	0.377	0.792
DD	-0.397	0.082	0.611	0.210	0.381	0.928
EE	-0.317	-0.052	0.237	0.116	0.826	0.943
FF	-0.324	-0.102	0.238	0.113	0.490	0.595
GG	-0.346	-0.029	0.252	0.071	0.269	0.630

Table 4: Test 2. Transects A-A to G-G. Statistical parameters.

	BIAS		RMSE		AI	
	CW	BSS	CW	BSS	CW	BSS
AA	0.022	0.075	0.119	0.140	0.993	0.990
BB	-0.029	0.047	0.150	0.249	0.979	0.940
CC	0.000	0.074	0.155	0.255	0.957	0.898
DD	-0.026	0.071	0.223	0.246	0.912	0.843
EE	0.022	0.028	0.126	0.147	0.979	0.967
FF	0.029	0.022	0.089	0.087	0.931	0.936
GG	0.032	0.036	0.048	0.105	0.587	0.182

Table 5: Test 3. Transects A-A to G-G. Statistical parameters.

In general, for all tests, the numerical model BOUSS-WMH can reproduce fairly well the behaviour and the magnitude of the experimental results. Indeed, the numerical model simulates the wave height growth over the shoal and close to that, and then the progressive wave height decrease (as it can be seen in transect A-A) as the wave moves away from the shoal.

In the other transects, the numerical values follow also the experimental ones, although there are major differences in the area after the shoal. Note that transects B-B, C-C, D-D are downstream the shoal, where nonlinearity effects are higher. Notice that BOUSS-WMH is a weakly nonlinear model. In transects F-F and G-G, the agreement index is lower which may be due to the low number of measuring points.

Specifically, with respect to test 1, (see Fig. 6 and Table 3) and in most transects, the model tends to underestimate the significant wave heights. The *bias* parameter graph clearly shows this trend. Only in transects F-F and G-G, the model overestimated the experimental results. The *rmse* is low in the sections E-E and G-G but reaches higher values in section B-B. The agreement index is over 0.7 in most transects, apart from transects B-B, C-C and G-G.

With respect to test 2 (see Fig. 7 and Table 4) the model reproduces well the wave height in all transects. This can be confirmed by the values of *rmse* and of the agreement index Fig.s. The *rmse* is lower than the test 1 and never exceeds 0.4. The index of agreement is always above 0.7 in all transects for both models except for the transect B-B and G-G. Regarding the *bias*, the model shows a different behaviour depending on the transect. In transects B-B, C-C and D-D the model overestimates the experimental results. In other transects, the reverse happens. Transect A-A both models underestimate the experimental values..

The analysis of test 3 (see Fig. 8 and Table 5) shows that BOUSS-WMH results tend to over-estimate of significant wave height for all transects, especially at transect A-A. The *bias* parameter graph clearly shows this trend. The agreement index is over 0.9, with the exception of transect G-G, transverse to the wave direction of the wave and on the front of the shoal, where the indexes were very small. The small values of the wave height and the few wave gauges may contribute to the value of *ic*. The biggest *rmse* was achieved at the D-D, just downstream from the shoal, where one expects a considerable transformation of the wave. Possibly, this results from a model limitation to represent higher harmonics present in this region.

Clearly, it appears that both models reproduce more accurately test 3 than test 2 and especially test 1. Note that this test is the least nonlinear of the tests simulated here.

3.1.3.3. Spectral analysis

Energy spectra were obtained at three different gauges located in the longitudinal section A-A for the three tests examined (Fig. 9 to Fig. 11). The gauges positions were x = 3.12 m and 7.42 m, known as gauges 1 and 9, respectively. The gauge 1 is upstream of the shoal, while the other is located downstream of it.

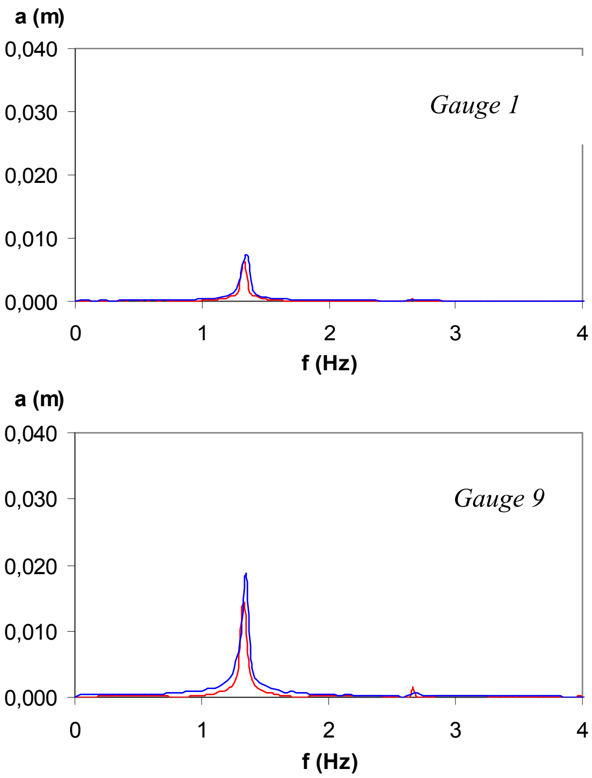

Fig. 9 – Test 1. Wave spectra. COULWAVE (blue) e BOUSS-WMH (red)

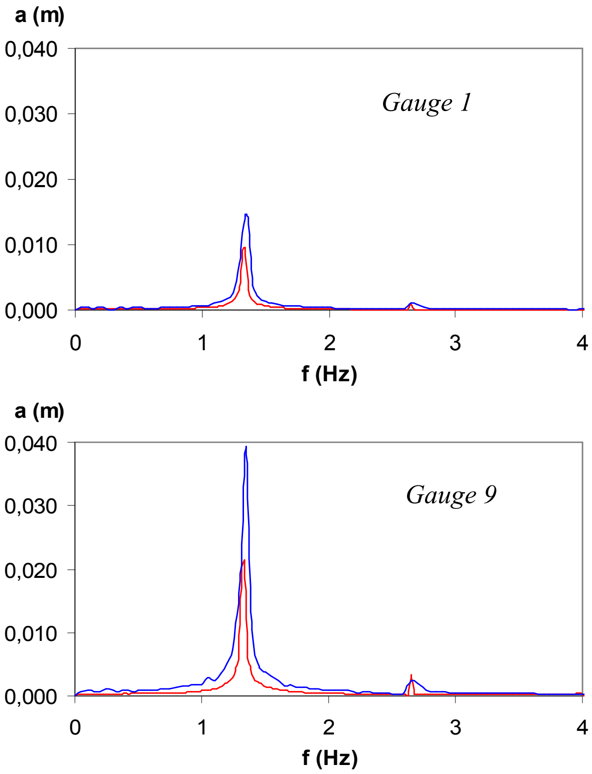

Fig. 10 - Test 2. Wave spectra. COULWAVE (blue) e BOUSS-WMH (red)

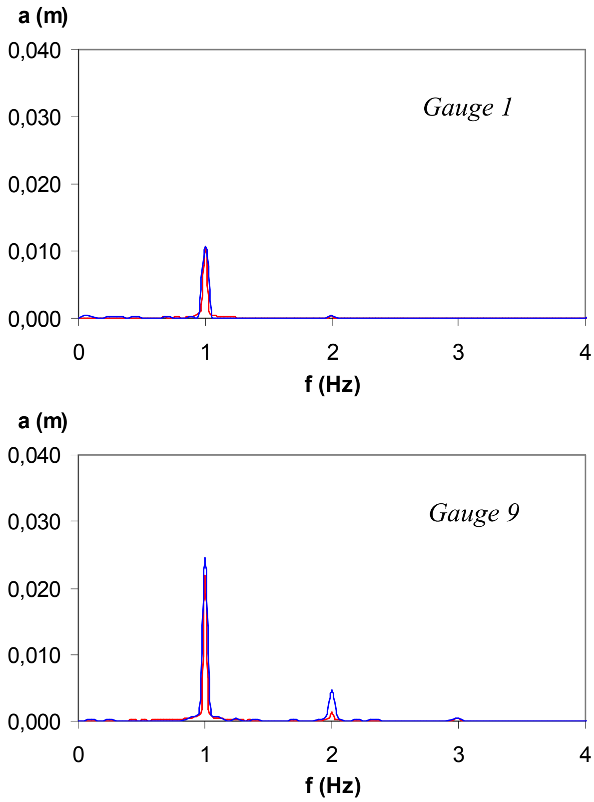

Fig. 11 - Test 3. Wave spectra. COULWAVE (blue) e BOUSS-WMH (red)

It is observed that as the wave propagates along the tank, the energy which was concentrated in only one frequency moves to other frequencies (harmonics) as expected. In all test cases, the second harmonic is associated with the higher energy, and especially at wave gauge 9. This is justified because this wave gauge is located closer to the shoal and downstream, where it expects higher nonlinearity.

Test 2 showed the presence of higher harmonics with higher intensity, which can be explained by the characteristics of the incident wave: the wave height is the largest of the test cases (H = 0.04m) and the wave period is shorter than test 3. Since the models are based on the Boussinesq equations, they are limited to relatively low values of *kh*. So, it can show some difficulty on simulating the third harmonic because they have values of *kh* in the range 16 to 50, see Table 1.

3.2Constant Slope Beach Profile

First, a calibration of the wave breaking parameters is performed by using one of the test conditions used on the experiments performed by Hansen & Svendsen [15], which simulate the wave propagation over a constant slope bottom. Once the best parameters were defined, the numerical model is applied to the other test conditions.

3.2.1 Numerical conditions

The model was applied to a simple case of wave propagation and breaking of regular waves over a constant slope beach profile for witch there are experimental results obtained by Hansen & Svendsen [15].

Wave are generated at a 0.36m depth and shoal on a 1:34.26 slope until they brake. Test cases number 031041, 041041 e 051041 from Hansen & Svendsen [15], experiments were reproduced in this work wich correspond to the wave characteristics in Table 6.

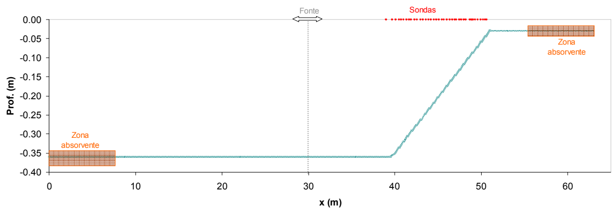

Fig. 12 - Bathymetry and location of source, sponge layers and wave gauges.

Test	Period (s)	Wave Height (cm)
031041	3.33	4.30
041041	2.50	3.90
051041	2.00	3.60

Table 6: Characteristics of generated waves.

The simulation time was of 40s. The numerical domain has 63m in length and the source is located at x=30.0 m. Two sponge layers were placed at the extremities. The domain was discretized with 4816 finite elements with 0.09m spacing between nodes. Over the slope 35 wave gauges were placed to measure wave heights. In order to avoid numerical instabilities the viscosity parameter was 3.0×10^{-3}, for cases 031041 e 0341041 and 2.2×10^{-3} for case 051041

3.2.2 Parameter calibration

Since experimental results are available the calibration of the several wave breaking parameters was made in order to get the best possible results. Parameters for the initiation and cessation of breaking are the most influential on the results while the other parameters have little influence.

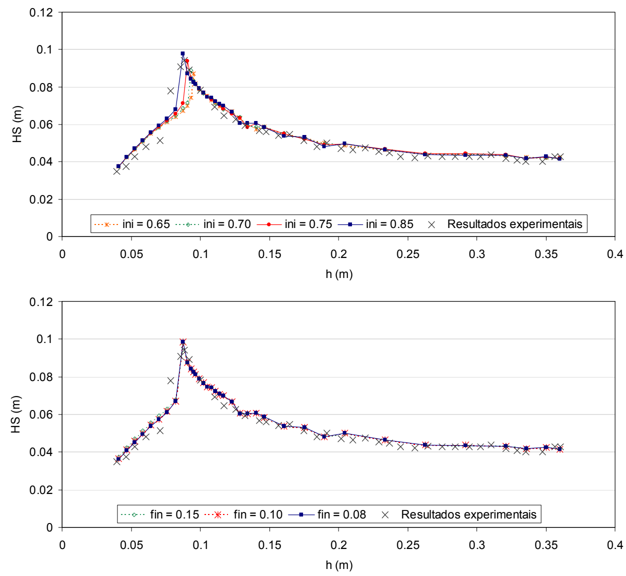

Fig. 13 - Calibration of initiation and cessation of wave breaking parameters for test 031041.

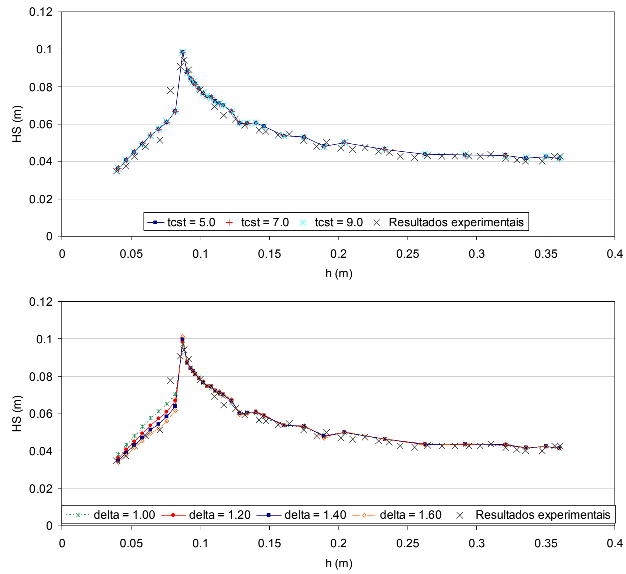

Fig. 14 - Calibration of transition time and mixing length coefficients for test 031041.

After analyzing these results the parameters adopted were:

$$\frac{\partial\eta^{(I)}}{\partial t}=0.85\sqrt{g.H_a} \quad \frac{\partial\eta^{(F)}}{\partial t}=0.08\sqrt{g.H_a} \qquad (32)$$
$$T^*=5.0\sqrt{H_a/g} \quad \delta_b=1.20$$

3.2.3 Results

Figure 4 and Figure 5 present the numerical and experimental results obtained for each incident wave condition. In general, for all cases tested, the numerical results follow well the experimental values, before and after breaking takes place. Indeed, for each test case, the wave shoals due to decreasing depth and brakes at the same locations obtained in experimental tests. After wave breaking occurs the wave height decreases due to

energy dissipation resulting from the turbulent phenomenon.
However, there are some differences; the energy dissipation of the numerical model is higher in case 031041 and especially in case 051041. In the case 041041 the breaking does not occur at the same depth.

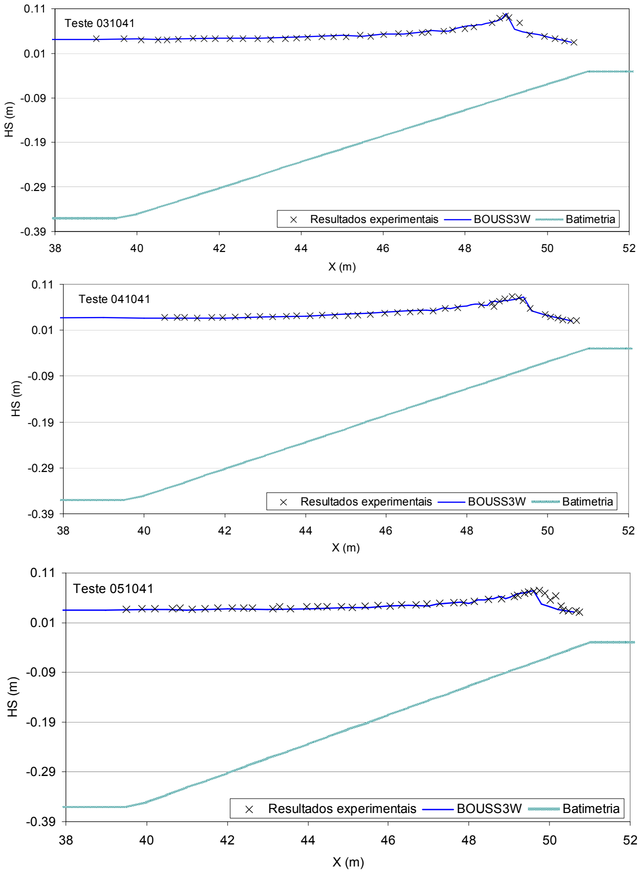

Fig. 15: Significant wave heigths HS (m) over the bathymetry for test cases 031041, 041041 and 051041.

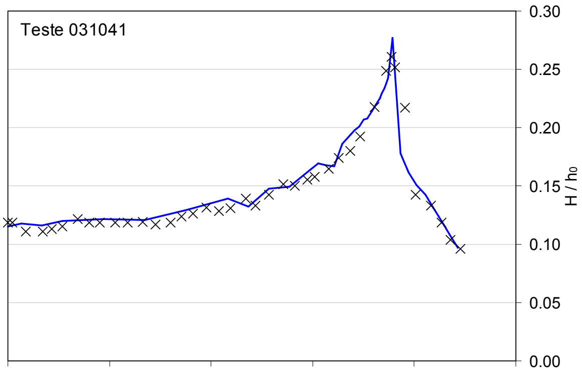

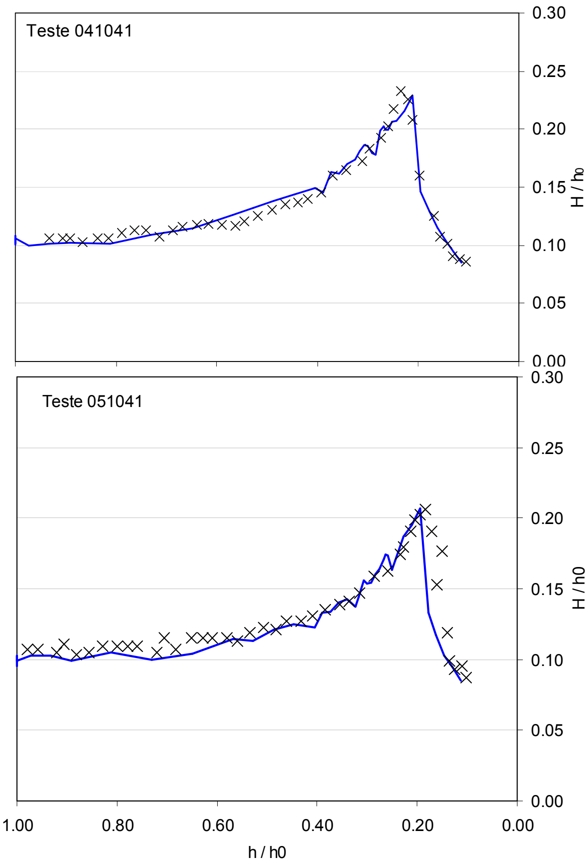

Fig. 16: Non dimensional wave heights for test cases 031041, 041041 and 051041.
The main conclusions of this test were:

- The model correctly simulates the behavior of the wave propagation along the domain;
- The model correctly predicts the wave height before wave breaking, and the energy dissipation after this, although it is slightly higher than that observed experimentally;
- The position of the break was well simulated by the numerical model, with only a slight difference in depth. In any case these differences are very dependent upon the test case.

3.3 Bared Beach Profile

This test case helps to evaluate the benefits of accounting for wave breaking related energy dissipation when studying real near shore and beach bathymetries.
A bared beach case has been done to check the behavior of the model when several wave breakings occur. This corresponds to an experimental study performed by Sancho *et al.* [37].

3.3.1 Numerical conditions

The bathymetry is 119.6 long, Fig. 17.

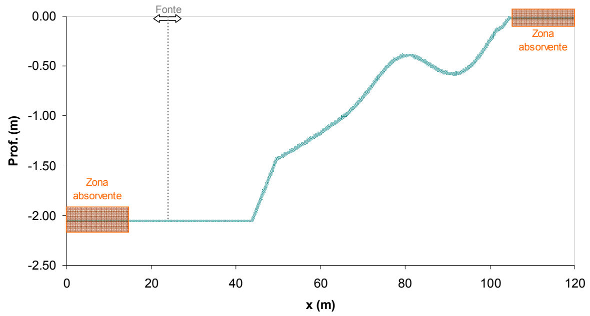

Fig. 17: Wave breaking test of a bared beach: Shape of the bathymetry.

The initial amplitude was 0.056m and a small viscosity of 2.0x10-3 was put in order to avoid all numerical instabilities. The period was 2.5s and the source function of was at x = 26.0m.

The domain was discretized by linear finite elements with two nodes and the spacing between two nodes was Δx = 0.05m. The corresponding domain has 2393 nodes. The simulation lasted 70s. Along the slope, 43 gauges were considered.

3.3.2 Parameter calibration

The first parameter to be calibrated is the numerical viscosity because it guarantees the stability of the numerical method but should not affect the results quantitatively. Therefore it should be as small as possible within the range allowing a stable run until the end of the simulation. Hence the value of this parameter decreased until the optimal value is found. values of 5×10^{-3}, 4×10^{-3}, 3×10^{-3}, 2×10^{-3} and 1×10^{-3} were tested, Fig. 18. Since the latter has failed to control the numerical instability the value adopted was 2×10^{-3}.

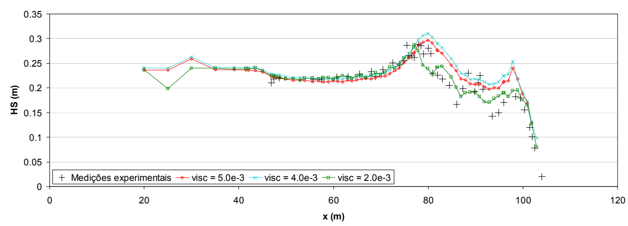

Fig. 18: Calibration of numerical viscosity parameter.

Subsequently some sensitivity tests were carried out to assess the influence of the wave breaking parameters and since experimental results were available it was possible to calibrate them.

The initiation of breaking parameter is one of the most important because it allows us to determine the location of the 1st breaking, which can significantly alter the subsequent results. Fig. 19 represents the values of wave height for the initiation breaking parameter ranging from 0.40 to 0.65. A statistical analysis showed that the value of 0.50 leads to a closer match between numerical and experimental results, Fig. 20.

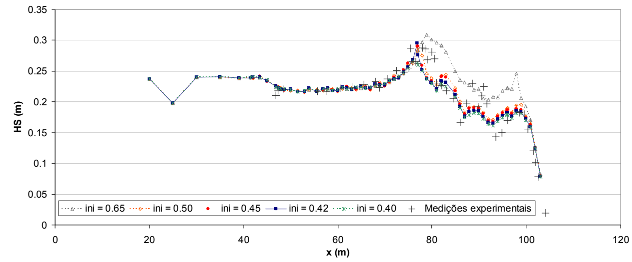

Fig. 19: Calibration of initiation parameter.

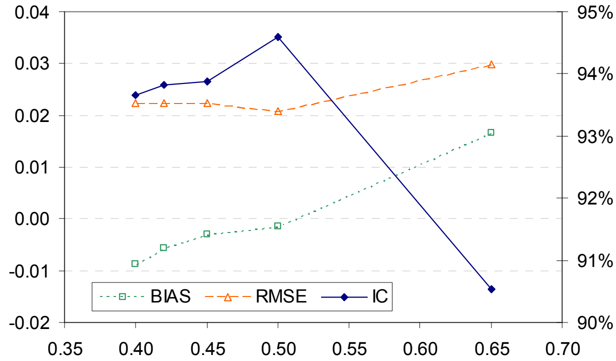

Fig. 20: Error statistics for the calibration of initiation parameter.

The cessation parameter was varied between 0.08 and 0.15 but it can be seen that it changes very little the results. The more appropriate in this case was 0.15, Fig. 21.

The same applies to the transition time and the mixing length coefficient that have little influence on the results.

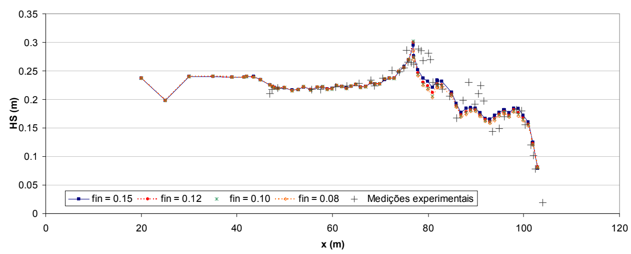

Fig. 21: Calibration of cessation parameter.

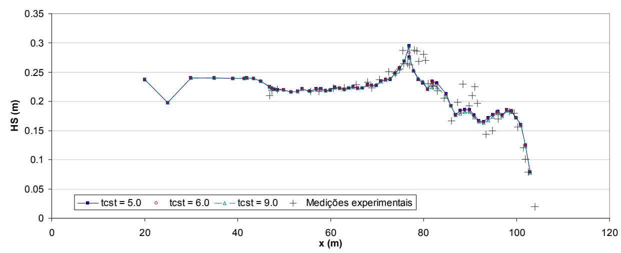

Fig. 22:Calibration of transition time.

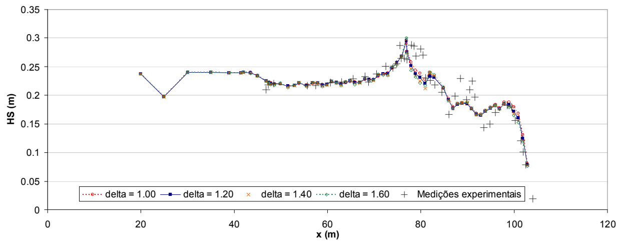

Fig. 23: Calibration of mixing length coefficient.

After analyzing these results the parameters adopted were:

$$\frac{\partial \eta^{(I)}}{\partial t} = 0.50\sqrt{g.H_a} \quad \frac{\partial \eta^{(F)}}{\partial t} = 0.15\sqrt{g.H_a}$$
$$T^* = 5.0\sqrt{H_a/g} \qquad \delta_b = 1.20 \tag{33}$$

3.3.3 Results

Fig. 24 represents the free surface elevation at the time instants 20s, 26s, 30s, 34s, 38s and 42s that correspond to the time interval in which the first fully developed waves reach the end of the beach. In these graphs it can be seen the wave travelling over the bar, breaking and then recover over the pit and break again on the beach (the latter phenomenon is most visible in the last plot at t = 42s).

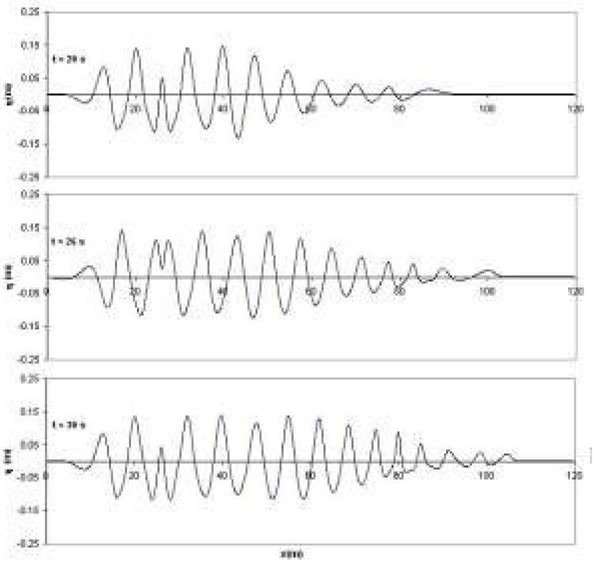

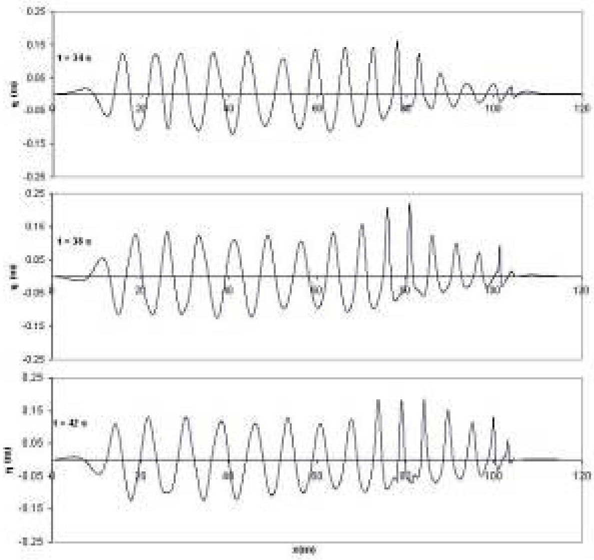

Fig. 24: Free surface elevation at several time instants.

Fig. 25 presents the comparison between the wave height experimental data and numerical results along the bathymetry obtained with BOUSS-WMH model and the FUNWAVE model. FUNWAVE **Error! Reference source not found.** is a phase-resolving, time-stepping Boussinesq model for ocean surface wave propagation in the near shore and the comparison of both results on the bared beach case is interesting. This model is more complex than BOUSS3W, however the formulation of breaking itself is very similar and previously tested. Both of models give results at the same gauges as the ones of experimental work.

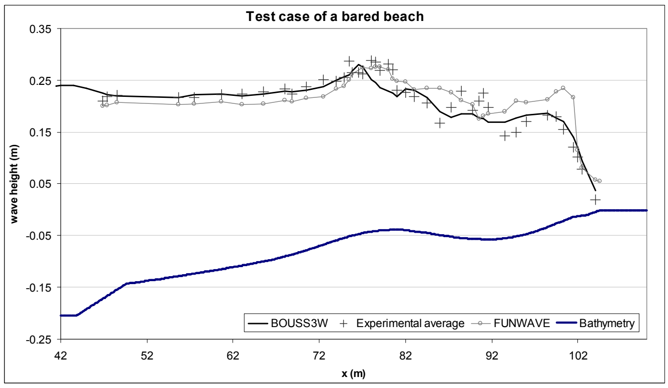

Fig. 25: Bathymetry and wave heights of the BOUSS-WMH and FUNWAVE models and experimental data.

BOUSS-WMH model reproduced very well the behavior of waves up to the wave breaking location, which has occurred slightly before the experimental one. Little differences can be noticed around 90.0m, but the last wave breaking is very well re-produced.

Although the BOUSS-WMH model seemed to be more accurate then FUNWAVE, computation of the

BIAS, the root mean square error (*RMSE*) and the index of agreement (*AI*) has been done in order to strictly compare the two numerical models, see Table 7.

	BIAS	RMSE	AI
BOUSS-WMH	-0.00419	0.0344	0.953
FUNWAVE	0.000164	0.0452	0.922

Table 7: Statistics of results.

A negative bias for BOUSS-WMH means that the model tends to underestimate the wave height, while the FUNWAVE's bias signifies that it overestimates it. Both of the values are very small. The root mean square error and the index of agreement show very good results from both models.

4. Conclusions

This paper describes the BOUSS-WMH model.

Previous applications of the model confirmed that the model was able to simulate quite well the main characteristics of the wave field outside and inside harbor configurations. However, important physical processes were not simulated, namely wave breaking. This phenomenon constitutes an important form of energy dissipation that cannot be neglected in near shore areas.

All the enhancements made for the BOUSS-WMH model improve its capacity to reproduce in a more realistic way phenomenon involved near coastal zone. It permits now to manage with full absorption and full or partial reflection boundary conditions, bottom friction and wave breaking events.

The results and comparisons with physical model tests data showed that:

- The physical processes introduced were adequately implemented in the model;
- The model was able to simulate correctly the wave propagation and most of the wave transformations present;
- There is a very good agreement with measured data.

In sum it can be concluded that BOUSS-WMH model is a powerful tool to characterize wave fields in near shore areas and more importantly with complex harbor geometries.

5. Acknowledgment

Financial support from the "Fundação para a Ciência e Tecnologia" (FCT) of the Ministry of Science and High Education of Portugal, through projects PTDC/ECM/73145/2006 and PTDC/ECM/67411/2006 are gratefully acknowledged.

References:

[1] Agnon, Y.; Madsen, P.A.; Schäffer, H. A new approach to higher order Boussinesq models. *J. Fluid Mechanics*, 399:319-333. 1999.

[2] Ambrosi. D. A new finite element scheme for the Boussinesq equations. *Mathematical Models and Methods in Applied Sciences*, 7(2):193–209. 1997.

[3] Antunes do Carmo J.S. & Seabra Santos F.J. On breaking waves and wave-current interaction in shallow water: a 2DH finite element model. *International Journal for Numerical Methods in Fluids*, vol. 22, 429-444.

[4] Beji, S.; Battjes, J.A. Numerical simulation of nonlinear-wave propagation over a bar. *Coastal Engineering,* 23(1-2):1–16. 1994.

[5] Beji, S.; Nadaoka, K. A formal derivation and numerical modeling of the improved Boussinesq equations for varying depth. *Ocean Engineering,* 23(8):691-704. 1996.

[6] Brown P.N., Hindmarsh A.C., and Petzold L.R.. Using Krylov methods in the solution of large-scale differential-algebraic systems. *SIAM Journal on Scientific Computing,* 15(6):1467–1488, 1989.

[7] Chawla A., *Wave transformation over a submerged shoal.* Master Thesis. University of Delaware, 1995.

[8] Chen Q., Kirby, J.T., Darymple, R.A., Kennedy, A.B. & Chawla, A. Boussinesq modeling of wave transformation, breaking and runup. II: Two Horizontal Dimensions. *J. Waterway, Port, Coastal and Ocean Engng.* 126: 48-56. 2000.

[9] Cuthill, E.; McKee, J. Reducing the bandwidth of sparse symmetric matrices. In *Proceedings of the 1969 24th national conference,* pages 157-172, New York, NY, USA,. ACM Press. 1969.

[10] Dietrich W. E. Settling Velocity of Natural Particles. *Water Resources Research*, Vol. 18, No. 6, pp1615-1626. December. 1982.

[11] Engelund, F.A. *On the laminar and turbulent flows of ground water through homogeneous sand.* Danish Academy of Technical Sciences. 1953.

[12] Eskilsson, C.; Sherwin, S.J.; Bergdahl, L. (2006 An unstructured spectral/hp element model for enhanced Boussinesq-type equations. *Coastal Engineering* 53 947–963. 2006.

[13] Gobbi, M.F.; Kirby, J.T. A fourth order fully non-linear Boussinesq wave model. *Proc. 25th*

International Conference on Coastal Engineering, Orlando, USA, 1, pp. 1116-1129. 1996.

[14] Grasselli, M.; Perotto, S.; Saleri, F. *Space-time finite elements for Boussinesq equations.* Technical Report 294/P, Department of Mathematics. Politecnico di Milano. 1997.

[15] Hansen, J. Buhr & I.A. Svendsen. *Regular waves in shoaling water. Experimental data.* Series Paper No 21, Inst. Hydrodyn. and Hydraulic Engrg., Techn. Univ. of Denmark, 1979, 20 + 223 pp.

[16] Katopodes, N.D.; Wu, C. Computation of finite-amplitude dispersive waves. *ASCE Journal of Waterway, Port, Coastal, and Ocean Engineering,* 113(4):327–346. 1987.

[17] Kennedy A. B., Chen Q., Kirby J. T., Dalrymple R. A. Boussinesq Modeling of Wave Transformation, Breaking, and Runup. I: 1D. *J. Waterway, Port, Coastal, and Ocean Eng.* P. 39-47, 2000.

[18] Kennedy, A.B.; Kirby, J.T.; Chen, Q.; Dalrymple, R.A. Boussinesq-type equations with improved nonlinear performance. *Wave Motion* 33 (3):225–243. 2000.

[19] Kirby, J.T. Nonlinear , Dispersive Long Waves in Water of Variable Depth. In J.N. Hunt (ed), Gravity Waves in Water of Variable Depth. *Advances in Fluid Mechanics.* 10: 55-125. Computational Mechanics Publications. 1997.

[20] Kirby, J.T.; Wei, G.; Chen, Q.; Kennedy, A. B.; Dalrymple, R. A. *FUNWAVE 1.0 – Fully Nonlinear Boussinesq Wave Model Documentation and User's Manual.* Research Report No.CACR-98-06. Center for Applied Coastal Research, University of Delaware. 1998.

[21] Le Roux, J.P., A simple method to predict the threshold of particle transport under oscillatory waves. *Sedimentary Geology* 143 (2001): 59–70—Reply to discussion. 2001.

[22] Li, Y.S.; Liu, S.-X.; Yu, Y.-X.; Lai, G.-Z. Numerical modeling of Boussinesq equations by a finite element method. *Coastal Engineering,* 37:97-122. 1999.

[23] Lynett, P. *A Multi-Layer Approach to Modeling Generation, Propagation, and Interaction of Water Waves.* PhD Thesis. Cornell University, August. 2002.

[24] Madsen, P.A.; Bingham, H.B.; Liu, H. A new Boussinesq method for fully nonlinear waves from shallow to deep water. *J. Fluid Mech.* 462:1–30. 2002.

[25] Madsen, P.A.; Fuhrman, D.R.; Wang Benlong A Boussinesq-type method for fully nonlinear waves interacting with a rapidly varying bathymetry. *Coastal Engineering,* 53:487-504. 2006.

[26] Madsen, P.A.; Murray, R.; Sørensen, O.R. A new form of the Boussinesq equations with improved linear dispersion characteristics. *Coastal Engineering,* 15:371–388. 1991.

[27] Madsen, P.A.; Schäffer, H.A. *Higher order Boussinesq-type equations for surface gravity waves – Derivation and analysis.* Phil. Trans. Roy. Soc., Series A, London, 356:3123-3184. 1998.

[28] Madsen, P.A.; Schäffer, H.A. *A review of Boussinesq-type equations for gravity waves.* Report pp. 1-63. 1998.

[29] Madsen, P.A.; Sørensen, O.R. A new form of the Boussinesq equations with improved linear dispersion characteristics. Part 2: A slowly-varying bathymetry. *Coastal Engineering,* 18:183-204. 1992

[30] Nwogu, O. Alternative form of Boussinesq equations for near-shore wave propagation. *J. Waterway, Port, Coastal, and Ocean Engineering,* 119(6), pp. 9-6, pp. 618 638. 1993.

[31] Nwogu, O. e Demirbilek, Z. *BOUSS-2D: A Boussinesq Wave Model for Coastal Regions and Harbors. Report 1 Theoretical Background and User.s Manual,* ERDC/CHL TR-01-25, U.S. Army Corps of Engineers. 2001.

[32] Peregrine, D.H. Long waves on a beach. *J. Fluid Mechanics* 27, pp. 815-827. 1967.

[33] Pinheiro L.V., Virginie Rodriguez, Fortes C. J., Teixeira P.R., Walkley M.A. BOUSS-WMH Nonlinear Wave Propagation Model. Bottom Friction Implementation. *7th European Conference on Computational Fluid Dynamics ECCOMAS CFD 2010* Lisbon, Portugal, 14–17 June 2010.

[34] Pinheiro, L., Fernandes, J.L.M., .Fortes, C.J. E.M. Finite Element Mesh Generator with Local Density Conditioned to Bathymetry for Wave Propagation Models in Coastal Zones. *IMACS Series in Comp. and Applied Mathematics* Vol.12, pp71-80. 2007.

[35] Pinheiro, L., Palha, A., Fortes, C. and Walkley Internal wave generation on finite element model BOUSS1D_iw: comparison with experimental data. *Proceedings of the Sixteenth International Offshore and Polar Engineering Conference* Lisbon, Portugal, July 1-6, 2309-2316. 2007.

[36] Saad Y. Iterative Methods for Sparse Linear Systems. *PWS,* 1996.

[37] Sancho F.E., Mendes P.A., Carmo J.A., Neves M.G., Tomasicchio G.R., Archetti R., Damiani L., Mossa M., Rinaldi A., Gironella X. And Sanchez-Arcilla A. Wave hydrodynamics over a barred beach. *Proceedings of the fourth International Symposium on Ocean Wave Measurement and Analysis - Waves*, San Francisco, ASCE, 1170-1179, 2001.

[38] Seeling, W.N. and J.P. *Ahrens Wave forces on inclined and vertical structures.* ASCE, pp.28-55. 1995.

[39] Walkley, M., Berzin, M., A finite element method for the one-dimensional extended Boussinesq equations, *Int. J. Numer. Meth. Fluids,* 29: 143-157. 1999.

[40] Walkley, M.; Berzins, M. A finite element method for the two-dimensional extended Boussinesq equations. *International Journal for Numerical Methods in Fluids,* 39(2):865–885. 2002.

[41] Wei, G., Kirby, J. T., Sinha, A. Generations of waves in Boussinesq models using a source function method, *Coastal Eng.,* 36(4), 271-299. 1999.

[42] Wei, G.; Kirby, J.T.; Grilli, S.T.; Subramanya, R. A fully non linear Boussinesq model for surface waves. Part 1. Highly non-linear unsteady waves. *J. Fluid Mechanics*, 294:71-92. 1995.

[43] Wei. G., Kirby. J. T., Grilli. S.T.& Subramanya R. A time-dependent numerical code for extended Boussinesq equations, *J. Waterway, Port, Coastal Ocean Engng.* 120: 251-261. 1995.

[44] Willmott, C.J., S.G. Ackleson, R.E. Davis, J.J. Feddema, K.M. Klink, D.R. Legates, J. O'Donnell e C.M. Rowe Statistics for the evaluation and comparison of models. *Journal of Geophysical Research*, 90 (c5), p. 8995-9005. 1985.

[45] Woo, S.-B.; Liu, P. L.-F. A Petrov–Galerkin finite element model for one-dimensional fully non-linear and weakly dispersive wave propagation. *Int. J. Numer. Meth. Fluids,* 37:541–575. 2001.

[46] Zou, Z.L. A new form of higher order Boussinesq equations. *Ocean Engineering,* 27:557–575. 2000.